

**AB-INITIO INVESTIGATION OF STRUCTURAL,
ELECTRONIC, AND ADSORPTION
PROPERTIES OF GRAPHITIC CARBON
NITRIDE SHEET WITH EMBEDDED
TRANSITION METAL Mn AND Fe ATOMS**

YUSUF ZUNTU ABDULLAHI

UNIVERSITI SAINS MALAYSIA

2018

**AB-INITIO INVESTIGATION OF STRUCTURAL,
ELECTRONIC, AND ADSORPTION
PROPERTIES OF GRAPHITIC CARBON
NITRIDE SHEET WITH EMBEDDED
TRANSITION METAL Mn AND Fe ATOMS**

by

YUSUF ZUNTU ABDULLAHI

**Thesis submitted in fulfilment of the requirements
for the degree of
Doctor of Philosophy**

June 2018

ACKNOWLEDGEMENT

I would like to extend my sincere gratitude to my supervisors, Dr. Mohd Mahadi Halim, Associate Prof. Dr. Yoon Tiem Leong, and Prof Md. Roslan Hashim for their helpful guidance, suggestions, swift feedback and support throughout my PhD study. Their scholarly scrutiny, criticisms, professional guidance and vision that kept me on the track when I got lost in the research work. Special thanks to my co-supervisor Associate Prof. Dr. Yoon Tiem Leong and Dr. Lim Thong Leng for the financial assistance. I have also benefited a lot from various theoretical discussion groups and workshop across Europe, one of which is PWSCF forum. In this regard, many thanks go to the moderator (who is ever ready to address any problem related to open source package (ESPRESSO)) and the contributors.

This research activity would have been more challenging without the immense moral support and encouragement of my parent, father, Alhaji Abdullahi Aliyu Zuntu and my mother, Hajiya Rabi'atu Tukur, who have always been there for me in all circumstances. Appreciation goes also to my fellow research group members for their support and friendly approach. I would also like to specifically thank Prof Mohd. Zubir Mat Jafri, School of Physics, and Dr. Chan Huah Yong from the School of Computer Science, USM, for their irreplaceable help for providing me computing resources to carry out the calculations done in this thesis. My warm regard goes to all colleagues at the university; friends and family back home for their unwavering supports and encouragement throughout the years of my PhD study. Special thanks to the entire Nigerian community in USM for the high standard of cooperation and brotherhood extended to me.

TABLE OF CONTENTS

Acknowledgement	ii
Table of Contents	iii
List of Tables	vii
List of Figures	x
List of Symbols	xvii
List of Abbreviations	xviii
Abstrak	xx
Abstract	xxiii

CHAPTER 1 – INTRODUCTION

1.0	Motivation	1
1.1	Pure Graphitic Carbon Nitride Sheet	5
1.2	Transition Metal Embedded Graphitic Carbon Nitride Sheet	8
1.3	Research Objectives	14
1.4	Scope and Limitation	15
1.5	Thesis Outline	16

CHAPTER 2 - THEORETICAL BACKGROUND AND METHODOLOGY

2.0	Introduction	17
2.1	Electronic Structure Calculations	17
2.1.1	Independent-electron Approximation	19
2.1.2	Hartree-Fock Approximation	20

2.1.3	Density Functional Theory (DFT)	21
2.1.4	Fundamentals of DFT	22
2.1.5	The Kohn-Sham (KS) Equations	24
2.1.6	The Exchange-Correlation Potential	26
2.1.7	The Approximation to the Exchange-Correlation Potential	27
2.1.8	Self-consistent Field Procedure for Kohn-Sham Equation	29
2.2	The Plane Wave Basis Sets	29
2.3	<i>k</i> -point Sampling	31
2.4	Atomic Pseudopotential Approximation	32
2.5	Introduction to Quantum Espresso	34
2.5.1	Types of Calculations in the Quantum Espresso	35
2.5.2	Geometry Optimization	37
2.5.3	Mechanical Properties	37
2.5.4	Electronic Density of State	39
2.6	The calculations procedure	40
2.6.1	Preliminary Convergences	43
2.6.2	Equilibrium Lattice Constant	45
 CHAPTER 3 - HEPTAZINE AND s-TRIAZINE SHEETS		
3.0	Introduction	47
3.1	Computational Methodology	47
3.2	Structural, Mechanical and Electronic Properties of Heptazine Sheet	49
3.3	Structural, Mechanical and Electronic Properties of s-triazine Sheet	62
3.3	Summary	72

CHAPTER 4 - Mn- AND Fe-EMBEDDED HEPTAZINE SHEET

4.0	Introduction	73
4.1	Computational Methodology	73
4.2	Structural, Mechanical, Electronic and Magnetic Properties of Mn-embedded Heptazine Sheet	76
4.3	Adsorption of Atoms on Mn-embedded Heptazine Sheet	89
4.4	Adsorption of Molecules on Mn-embedded on Heptazine Sheet	92
4.5	Structural, Mechanical, Electronic and Magnetic Properties of Fe-embedded Heptazine Sheet	95
4.6	Adsorption of Atoms on Fe-embedded Heptazine Sheet	104
4.7	Adsorption of Molecules on Fe-embedded on Heptazine Sheet	107
4.8	Summary	109

CHAPTER 5- Mn- AND Fe-EMBEDDED s-TRIAZINE SHEET

5.0	Introduction	111
5.1	Computational Methodology	111
5.2	Structural, Mechanical, Electronic and Magnetic Properties of Mn-embedded s-triazine Sheet	113
5.3	Adsorption of Atoms on Mn-embedded s-triazine Sheet	121
5.4	Adsorption of Molecules on Mn-embedded on s-triazine Sheet	123
5.5	Structural, Mechanical, Electronic and Magnetic Properties of Fe-embedded s-triazine Sheet	127
5.6	Adsorption of Atoms on Fe-embedded s-triazine Sheet	134
5.7	Adsorption of Molecules on Fe-embedded on s-triazine Sheet	137
5.8	Summary	140

CHAPTER 6 - CONCLUSION AND RECOMMENDATIONS

6.0 Conclusion 142

6.1 Recommendations 144

REFERENCES 146

LIST OF PUBLICATIONS

LIST OF TABLES

		Page
Table 3.1	The optimized lattice parameters and total energy of heptazine sheet and C – doped heptazine sheet for bulk modulus measurements	52
Table 3.2	Numerically evaluated mechanical properties of heptazine sheet as calculated based on the strain energy curves data in Fig. 3.4.	56
Table 3.3	The optimized lattice parameters and total energy of s-triazine sheet for bulk modulus estimations.	66
Table 3.4	Numerically calculated mechanical properties of s-triazine sheet obtained from the strain energy curves in Fig 3.10	67
Table 4.1	The optimized Lattice parameters and total strain energy of C_6N_7 – Mn system for mechanical properties measurement.	78
Table 4.2	The optimized geometric properties of the strained/unstrained C_6N_7 – Mn systems. The binding energies E_b , the average bond length between Mn adatom and N atom, average bond length linking the heptazine, the N – C – N, θ angle and Mn height are denoted as d_{Mn-N} , and d_1/d_1 , and, h (difference in the z -coordinate of the Mn atom and the average of the z -coordinate of all the C and N atoms in the C_6N_7 sheet), respectively. The charge transfer into the C_6N_7 sheet is based on Löwdin's charge analysis. Magnetic moment per unit cell and per Mn atom, electronic character of the C_6N_7 – Mn system and the approximate band gap are denoted by Q , M_{cell} , M_{Mn} , EC and BG, respectively.	80
Table 4.3	Structural and electronic parameters of the C_6N_7 – Mn systems with atom/molecule adsorbed after relaxation. E_{ads} denotes the adsorption energy. d_{Mn-X} is the bond length between Mn atom and the lowest atom in the adsorbates. d_X is the averaged bond length of molecules, where X denotes the adsorbate species. The values without parenthesis are that for absorbed molecules while that in parenthesis are for isolated molecules. Q denotes charge transfer among the adsorbates and the C_6N_7 – Mn system. Q values without parenthesis are charge transfer from Mn atom into the sheet or adsorbates. Positive $Q = +ve$ value means the electron is transferred into the surrounding, and	91

vice versa. $Q = \pm$ ve values in parenthesis are charge transferred/gained by the adsorbates into the surrounding. M_{cell} is magnetic moment per unit cell. M_{atom} denotes magnetic moment of Mn atom or adsorbates. Values without parenthesis are for the Mn atom, while that in parenthesis are for the adsorbates. EC denotes the electronic character of the $\text{C}_6\text{N}_7 - \text{Mn}$ with adsorbates. Metallic (M), half metallic (HM) and semiconducting (SC) denotes the electronic character found in these systems.

Table 4.4	Structural and electronic parameters of the $\text{C}_6\text{N}_7 - \text{Mn}$ systems with molecule adsorbed after relaxation. The notations are the same as that defined in Table 4.3. $d_{\bar{X}}$ is the averaged bond length ($d_{\text{C-O}}$, $d_{\text{C-O-O}}$, $d_{\text{O-O}}$, $d_{\text{N-N}}$, $d_{\text{H-H}}$, and $d_{\text{C-H-H-H-H}}$) of molecules, where X denotes the adsorbate species (CO , CO_2 , O_2 , N_2 , H_2 , CH_4). $d_{\text{Mn-X}}$ (e.g. $d_{\text{Mn-CO}}$, $d_{\text{Mn-CO}_2}$, $d_{\text{Mn-O}_2}$, $d_{\text{Mn-N}_2}$, $d_{\text{Mn-H}_2}$, and $d_{\text{Mn-CH}_4}$) is the bond length between Mn atom and the lowest atom in the adsorbates..	95
Table 4.5	Computed optimized lattice parameters, unit cell area and total energy of $\text{C}_6\text{N}_7 - \text{Fe}$ monolayer for elastic moduli measurement.	97
Table 4.6	Structural and electronic data for the strained/unstrained $\text{C}_6\text{N}_7 - \text{Fe}$ systems. The notations are the same as that defined in Table 4.3, Section 4.4.	98
Table 4.7	Structural and electronic parameters of the $\text{C}_6\text{N}_7 - \text{Fe}$ systems with atom adsorbed after relaxation. The notations are the same as that defined in previous Table 4.3, Section 4.4.	105
Table 4.8	Structural and electronic parameters of the $\text{C}_6\text{N}_7 - \text{Fe}$ systems with molecule adsorbed after relaxation. The notations are the same as that defined in previous Table 4.4, Section 4.4.	107
Table 5.1	Optimized lattice parameters and total strain energy of $\text{Mn} - \text{C}_6\text{N}_6$ system for mechanical properties computation.	114
Table 5.2	Structural and electronic data for the strained/unstrained $\text{C}_6\text{N}_6 - \text{Mn}$ systems. The notations are the same as that defined in Table 4.2, Section 4.4.	116
Table 5.3	Physical parameters of the $\text{Mn} - \text{C}_6\text{N}_7$ systems with atom adsorbed after relaxation. The notations are the same as that defined in Table 4.3, Section 4.4.	122

Table 5.4	Structural and electronic parameters of the $\text{Mn} - \text{C}_6\text{N}_6$ systems with atom adsorbed after relaxation. The notations are the same as that defined in Table 4.4, Section 4.4.	125
Table 5.5	Calculated lattice parameters and total strain energy for Fe atom embedded s-triazine system.	129
Table 5.6	Structural and electronic data for the strained/unstrained $\text{Fe} - \text{C}_6\text{N}_6$ systems. The notations are the same as that defined in Table 4.2, Section 4.4.	130
Table 5.7	Structural and electronic parameters of the $\text{Fe} - \text{C}_6\text{N}_7$ systems with atom adsorbed after relaxation. The notations are the same as that defined in Table 4.3, Section 4.4.	135
Table 5.8	Structural and electronic parameters of the $\text{Fe} - \text{C}_6\text{N}_7$ systems with molecule adsorbed after relaxation. The notations are the same as that defined in Table 4.4, Section 4.4.	137

LIST OF FIGURES

		Page
Figure 1.1	Primitive cells of 4-dense C_3N_4 phases: (a) $\alpha - C_3N_4$, (b) $\beta - C_3N_4$, (c) cubic $- C_3N_4$ and (d) pseudocubic $- C_3N_4$. Carbon and nitrogen atoms are depicted in big and small balls, respectively [16]. (e) graphitic $- C_3N_4$.	6
Figure 2.1	Self-consistent algorithms for solving Kohn-Sham [4].	28
Figure 2.2	The convergence of total energies as a function of cut-off energy for nitrogen atom.	31
Figure 2.3	The convergence of total energies as a function of k -points for primitive unit of s-triazine sheet.	32
Figure 2.4	Schematic representation of pseudopotential (solid lines) and all-electrons (dash lines) potentials with their corresponding wave functions. The radius at which the pseudo-electron and all-electron values match is denoted as r_c [85].	33
Figure 2.5	Schematic diagram of DFT calculation procedure (Quantum Espresso package).	42
Figure 2.6	(a) The convergence of total energies of nitrogen (left) and carbon (right) as a function of cut-off energy. (b) The convergence of total energies of manganese (left) and iron (right) as a function of cut-off energy.	43
Figure 2.7	The convergence of total energies as a function of k -points for primitive unit of s-triazine sheet (Left) and 2x2 unit cell of Mn embedded s-triazine system (Right).	44
Figure 2.8	Equilibrium lattice constant for (a) Bulk heptazine (b) Bulk s-triazine (c) Mn embedded heptazine sheet (d) Fe embedded heptazine sheet (e) Mn embedded s-triazine sheet (f) Fe embedded s-triazine sheet.	46
Figure 3.1	Left: Top view of the $2 \times 2 \times 1$ optimized heptazine supercell. The atomic symbols and the calculated structural parameter are clearly labeled. Carbon atoms are in black, whereas nitrogen atoms in grey colour. The angles of $N - C - N$, θ , are also indicated. Right: A heptazine (or tri-single triazine-based $g - t - C_3N_4$) unit which is comprised of 3 C_3N_4 (triazine) rings. The lattice constant of 7.14 Å is also displayed.	48

Figure 3.2	(a) Top view of the charge-density distributions of the nearest neighbouring C and N atoms of a strain-free heptazine, with colours scale indicating ranges of charge accumulation and depletion in a.u. Carbon atoms are in black, whereas nitrogen atoms in grey colour. (a) Dependence of formation energy versus biaxial and uni-axial strains of the heptazine sheet.	50
Figure 3.3	(a) Variation of energy (Ry) versus uni-axial strain of the heptazine. (b) Variation of energy (Ry) versus bi-axial strain of the heptazine. (c) Variation of energy (Ry) versus the area (\AA^2) of the heptazine for bulk modulus measurement. (d) Variation of energy (Ry) versus the area (\AA^2) of the C – doped heptazine system for bulk modulus measurement.	51
Figure 3.4	Variation of strain energy versus strain, and variation of first derivative of strain energy versus strain of heptazine sheet. (a), (b) Uni-axial strain; (c), (d) bi-axial strain. The two critical points are labelled as C1 (green dot) and C2 (brow dot) in the figures. The dots are raw DFT data points obtained from the present calculation, while the continuous lines are best fit curves to these data points. The dotted curves are harmonic potentials fitted to the data points centered in the $\pm 2\%$ strain region.	58
Figure 3.5	The band structure, and the corresponding total and projected densities of state for the strained ($s = 3\%$) and strained-free ($s = 0$) heptazine systems. (a1) and (a2) Band structures for the heptazine systems respectively. (b1) and (b2) The total density of state (TDOS) heptazine systems. (c1)-(g1) The projected density of states (PDOS) for sp like-orbital of the sum of N_{bg} , N_{in} , N_{ed} , C_{bg} and C_{in} atoms in the heptazine strained-free systems respectively. (c2)-(g2) The projected density of states (PDOS) for sp like-orbital of the sum of N_{bg} , N_{in} , N_{ed} , C_{bg} and C_{in} atoms in the heptazine strained systems respectively.	55
Figure 3.6	(a) Band gap as a function of uniform bi-axial strain on pristine heptazine sheet. (b) The TDOS (Left) and the side view of the heptazine sheet (Right) under electric field of magnitude 10.0 V/nm.	61
Figure 3.7	Middle: Top view of the 1×1 s-triazine unit cell. The atomic symbols and the computed lattice constant of 7.14 \AA are well labelled. Left: The relaxed structure of 2×2 pure graphitic C_6N_6 sheet. Right: Top view of the charge-density distributions of the nearest neighbouring C and N atoms of an unstrained s-triazine sheet, with contours	63

indicating charge accumulation and colour ranges in a.u. carbon atoms are in black, whereas nitrogen atoms in grey colour.

Figure 3.8	Dependence of formation energy versus biaxial and uni-axial strains of the s-triazine sheet.	64
Figure 3.9	(a) The dependence of strain energy (Ry) on bi-axial tensile strain of the s-triazine sheet. (b) The dependence of strain energy (Ry) on uni-axial tensile strain of the s-triazine sheet. (c) The dependence of strain energy (Ry) on area (Angstrom ²) of the s-triazine sheet for bulk modulus estimation.	65
Figure 3.10	Dependencies of strain energy and derivative of energy on strain of s-triazine sheet. (a), (b) Uni-axial strain; (c), (d) bi-axial strain. The two critical points are labelled as C1 (circled star) and C2 (star) in the Figs. The insets in 3a and 3c are strain energy curves in harmonic elastic region. The dots are raw DFT data points computed in this work, while the continuous lines are best-fit curves to these data points. The dotted curves are harmonic potentials fitted to the data points cantered in the $\pm 2\%$ strain region.	67
Figure 3.11	The band structure, and the corresponding total and projected densities of state for the strained ($s = 3\%$) and unstrained ($s = 0$) s-triazine systems. (a) and (b) Band structures for the s-triazine systems respectively. (b) and (c) The total density of states (TDOS) for the s-triazine system. (e)-(h) The projected density of states (PDOS) for sp-like orbitals of the sum of N and C atoms in the s-triazine systems respectively. (i) The TDOS of the s-triazine sheet under electric field of magnitude 10.0 V/nm. (j) The dependence of band gap on uniform bi-axial tensile strain for s-triazine sheet.	71
Figure 4.1	Linear response of d orbital occupations to the change of potential shift α . The curves represented by the dotted and solid black lines are labelled I and II. The inverse response functions are derived numerically by determining the slope of the curves. χ_0 follows from the slope of curve I, whereas χ from the slope of curve II. 3.8 eV and 5.4 eV for (a) Mn and (b) Fe atoms, respectively.	75
Figure 4.2	Top view of the optimized $2 \times 2 \times 1$ structure of C_6N_7 with embedded Mn atom.	76
Figure 4.3	Strain energy (Ry) as a function of (i) bi-axial (ii) uni-axial and (iii) area of the Mn – CN system for elastic constant calculation.	77

Figure 4.4	Dependence of binding energy on the applied electric field for $C_6N_7 - Mn$ system.	82
Figure 4.5	Top view of the charge-density difference of the Mn atom and the nearest neighboring C and N atoms of a strain-free system, with colors scale indicating ranges of charge accumulation and depletion in a.u. Carbon atoms are in yellow. Atoms dotted with 4-point stars are the edge atoms (nitrogen atoms).	83
Figure 4.6	(a) Total density of states (TDOS) of bare C_6N_7 showing an indirect band gap in the vicinity of the Fermi level. (b) Band gap as a function of uniform bi-axial strain on bare C_6N_7 .	84
Figure 4.7	The plot of strain-dependent band gap of the $C_6N_7 - Mn$ system.	84
Figure 4.8	Spin-polarized band structure and the corresponding TDOS and PDOS for the unstrained ($s = 0$) $C_6N_7 - Mn$ system. (a) Majority spin state of the $C_6N_7 - Mn$ system. (b) Minority spin state of the $C_6N_7 - Mn$ system. (c) The spin-polarized TDOS of the $C_6N_7 - Mn$ system. (d) The spin-polarized projected density of states for sp like-orbital of the sum of 6 edge N atoms in the C_6N_7 with embedded Mn atom. (e) The spin-polarized projected density of states for sp-like orbitals of the Mn atom in the $C_6N_7 - Mn$ system. (f) The spin-polarized projected density of states for d-like orbitals of the Mn atom in the $C_6N_7 - Mn$ system.	85
Figure 4.9	Left: Side view of the optimized buckled $2 \times 2 \times 1$ structure of C_6N_7 with embedded Mn atom without applied perpendicular electric field. Right: Side view of the optimized buckled $2 \times 2 \times 1$ structure of C_6N_7 with embedded Mn atom under applied perpendicular electric field.	88
Figure 4.10	TDOS with an arrow indicating spin up and spin down directions of $C_6N_7 - Mn$ systems under applied electric field. (a) The spin-polarized TDOS for $C_6N_7 - Mn$ system under applied electric field of magnitude (i) 1.0 V/nm and (ii) 5.0 V/nm.	88
Figure 4.11	Side view and spin-polarized TDOS for $C_6N_7 - Mn$ with an adsorbed (a) C (b) N (c) O and (d) H atom.	90

Figure 4.12	Side view and spin-polarized TDOS for $C_6N_7 - Mn$ with an adsorbed (a) N_2 (b) H_2 (c) CO (d) CO_2 (e) O_2 and (f) CH_4 molecule.	93
Figure 4.13	Top view of a supercell comprised of 2×2 heptazine unit cell, with an embedded Fe atom. This 2×2 supercell is the one that was used as the input in our calculation.	96
Figure 4.14	Total energy (Ry) vs. area (\AA^2) of the $C_6N_7 - Fe$ system for bulk modulus calculations.	97
Figure 4.15	Dependence of binding energy on the applied electric field for $C_6N_7 - Fe$ and $C_6N_7 - Mn$ systems.	99
Figure 4.16	Top view plot of the charge-density difference of a supercell comprised of 2×2 heptazine unit cell with embedded Fe atoms. Charge depletion and localization in a.u. are depicted by colors scale $n(r)$. Carbon atoms are in black. Atoms dotted with 4-point stars are the nitrogen atoms in pink color.	100
Figure 4.17	(a) TDOS of pristine C_6N_7 with an arrow indicating spin up and spin down directions. There is an indirect band gap in the vicinity of the Fermi level. (b) TDOS with an arrow indicating spin up and spin down directions for $s = 5\%$ tensile strain $C_6N_7 - Fe$ system.	101
Figure 4.18	Spin-polarized electronic band structure and the corresponding TDOS and PDOS for unstrained ($s = 0$) $C_6N_7 - Fe$ system. (a) Spin up band structure of $C_6N_7 - Fe$ system. (b) Spin down band structure of $C_6N_7 - Fe$ system. (c) TDOS of the $C_6N_7 - Fe$ system with an arrow indicating spin up and spin down directions. (d) Projected density of states (PDOS) with an arrow indicating spin up and spin down directions for (i) sp like-orbital of the sum of 6 edge N atoms (ii) sp-like orbitals of the Fe atom in the $C_6N_7 - Fe$ system (iii) d-like orbitals of the Fe atom in the $C_6N_7 - Fe$ system, respectively.	102
Figure 4.19	Left: Side view of the optimized buckled $2 \times 2 \times 1$ structure of C_6N_7 with embedded Fe atom without applied perpendicular electric field. Right: Side view of the optimized buckled $2 \times 2 \times 1$ structure of C_6N_7 with embedded Fe atom under applied perpendicular electric field.	103
Figure 4.20	The spin-polarized TDOS with an arrow indicating spin up and spin down directions of $C_6N_7 - Fe$ system under electric field of magnitude (i) 1.0 V/nm (ii) 5.0 V/nm .	104

Figure 4.21	Side view and spin-polarized TDOS for $C_6N_7 - Fe$ with an adsorbed (a) C (b) N (c) O (d) H atom.	106
Figure 4.22	Side view and spin-polarized TDOS for $C_6N_7 - Fe$ with an adsorbed (a) N_2 (b) H_2 (c) CO (d) CO_2 (e) O_2 and (f) CH_4 molecule.	108
Figure 5.1	Linear response of d orbital occupations as a function of potential shift α . The curves depicted by the dotted red and black lines are labelled bare and interacting. The inverse response functions are deduced numerically by calculating the slope of the curves. χ_0 follows from the slope of curve bare, whereas χ from the slope of curve interacting.	112
Figure 5.2	Top view of a supercell comprised of 2×2 s-triazine unit cell, with an embedded Mn atom ($Mn - C_6N_6$). This $Mn - C_6N_6$ is the one that was used as the input in our calculation. There are six N_{6EG} (edge nitrogen atoms) of them around the cavity.	112
Figure 5.3	Dependence of strain energy (Ry) on (i) bi-axial (ii) uni-axial and (iii) area of the $Mn - C_6N_6$ system for elastic constant calculation.	113
Figure 5.4	(a) Top view plot of the charge-density difference of the Mn atom and the surrounding C and N atoms. The color scale shows ranges of charge accumulation and depletion in a.u. Carbon atoms are in black. Atoms dotted with 4-point stars are the N_{6EG} atoms (nitrogen atoms in dark ash color). (b) The spin-polarized total density of state (TDOS) for pure C_6N_6 .	117
Figure 5.5	Spin-polarized electronic band structure (a) majority (b) minority spin states for unstrained ($s = 0$) $Mn - C_6N_6$ system. Spin-polarized TDOS and projected density of state (PDOS) for strain-free (b)i-(f)I and strained (b)ii-(f)ii systems respectively.	118
Figure 5.6	(a) Side view of the optimized buckled $Mn - C_6N_6$ under applied perpendicular electric field. (b) The binding energy depicted by the dotted red and black lines respectively as a function of an applied electric field for $Mn - C_6N_6$ system. (c) The spin-polarized total density of state (TDOS) for $Mn - C_6N_6$ under applied electric field.	120
Figure 5.7	Spin-polarized TDOS and side view for $Mn - C_6N_6$ with an adsorbed (i) C (ii) N (iii) O and (iv) H atoms.	123

Figure 5.8	Spin-polarized TDOS and side view for Mn – C ₆ N ₆ with an adsorbed (i) N ₂ (ii) H ₂ (iii) CO (iv) CO ₂ (v) O ₂ and (vi) CH ₄ molecules systems, respectively.	126
Figure 5.9	Relaxed structure of 2×2 C ₆ N ₆ sheet (Left panel) and relaxed structure (Right) of Fe-embedded 2×2 C ₆ N ₆ (Fe – C ₆ N ₆).	128
Figure 5.10	The variation of strain energy (Ry) versus (i) bi-axial tensile strain (ii) uni-axial tensile strain and (iii) area of the Fe – C ₆ N ₆ system for elastic constant calculation.	130
Figure 5.11	Difference charge-density for Fe atom embedded s-triazine. The colour scale shows ranges of charge accumulation and depletion in a.u.	131
Figure 5.12	The spin-polarized total density of state (TDOS) for (i) pure s-triazine sheet (ii) Fe – C ₆ N ₆ under applied electric field. (iii) Variation of binding energy versus applied electric field strength for Fe – C ₆ N ₆ system.	132
Figure 5.13	Spin-polarized electronic band structure (a) majority (b) minority spin states for unstrained (<i>s</i> = 0) Fe – C ₆ N ₆ system. Spin-polarized TDOS and projected density of state (PDOS) for strain-free (c)-(f).	133
Figure 5.14	Spin-polarized TDOS and side view for Fe – C ₆ N ₆ with an adsorbed (a) C (b) N (c) O and (d) H atoms systems, respectively.	136
Figure 5.15	Spin-polarized TDOS and side view for Fe@C ₆ N ₆ with an adsorbed (a) N ₂ (b) H ₂ (c) CO (d) CO ₂ (e) O ₂ and (f) CH ₄ molecules systems, respectively.	140

LIST OF SYMBOLS

θ	Angle in Degree
H	Hamiltonian
ψ	Wavefunction
$n(r)$	Charge Density
$V(r)$	Potential
\mathbf{G}	Reciprocal Lattice Vector
a_0	Lattice Constant
Y	In-plane Stiffness
ν	Poisson's Ratio
G	Bulk Modulus
χ	Density Response Functions
α	Perturbation Potential
σ	Lone Pairs

LIST OF ABBREVIATIONS

BFGS	Broyden–Fletcher–Goldfarb–Shanno
BO	Born-Oppenheimer
C	Coulomb
CBM	Conduction Band Minimum
CN	Carbon Nitride
DFT	Density-Functional Theory
DOS	Density of States
GE	Gradient Expansion
GGA	Generalized Gradient Approximation
GGA + U	Generalized Gradient Approximation Plus Hubbard U
H	Hatree
HED	Homogeneous Electron Gas
HF	Hatree-Fock
HK	Hohenberg-Khon
HSE	Heyd-Scuseria-Ernzerhof
KS	Khon-Sham
LDA	Local-Density Approximation
LSDA	Local Spin-Density Approximation
MAE	Magnetic Anisotropy Energy
NEB	Nudged Elastic Band
PBE	Perdew-Burke-Ernzerhof of GGA
PDOS	Partial Density of States
PWSCF	Plane Wave Self-Consistent Field
PW91	Perdew-Wang 91 GGA

QE	QUANTUM ESPRESSO
Ry	Rydberg
TF	Thomas-Fermi
TM	Transition Metal
SAC	Single Atomic Catalyst
SCCM	Standard Cubic Centimeters per Minute
SR	Scalar-Relativistic
STM	Scanning Tunneling Microscope
VBM	Valence Band Maximum
XC	Exchange-Correlation

**PENYIASATAN AB-INITIO SIFAT STRUKTUR, ELEKTRONIK, DAN
PERJERAPAN HELAIAN KARBON NITRIDA GRAFIT TERBENAM
DENGAN ATOM LOGAM PERALIHAN Mn DAN Fe**

ABSTRAK

Pada masa kini, minat kajian terhadap nanostruktur magnetik terarah pada pencarian substrat yang sesuai untuk pengkapsulan atom logam peralihan (TM). Substrat yang bersesuaian adalah dijangka dapat mengekalkan sifat intrinsiknya serta atom TM yang terlibat. Graphene dan permukaan dengan gegelung segienam seragam padat sering menjadi pilihan untuk memerangkap atom-atom TM disebabkan sifat permukaan yang dikehendaki. Walaubagaimanapun, laporan menunjukkan yang atom-atom TM terikat dengan mudah diatas permukaan 2D ini disebabkan oleh tenaga penjerapan yang rendah. Bagi memastikan ketakmobilitian atom-atom TM atas permukaan tersebut, banyak usaha telah dilakukan bagi mensintesis bahan 2D yang tersedia dengan rongga sekata sebagai contoh, karbon nitrida (CN). Penyiasatan sifat fizik yang intensif telah dijalankan keatas helaian CN grafit tulen dan yang terdop semenjak beberapa tahun dahulu. Walaubagaimanapun, sifat fizik bagi CN grafit tulen dan yang terdop di bawah usikan luaran masih terselindung. Menggunakan kaedah prinsip pertama berdasarkan teori fungsi ketumpatan (DFT), dan berbantuan pakej QUANTUM ESPRESSO, sifat fizik keadaan asas bagi kedua-dua kes tulen dan TM terbenam dalam helaian-helainan heptazina dan s-triazina dibawah terikan mekanik, medan elektrik, dan penjerapan kimia telah dikaji. Keputusan menunjukkan yang helaian heptazina dan s-triazina adalah stabil secara struktur dan mekanik. Nilai yang dikira bagi terikan genting (pekali perkadaran dan titik keluluhan) menunjukkan

helaian s-triazina boleh menanggung tegangan yang besar dalam rantau elastik lurus lebih dari helaian heptazina dan kedua helaian boleh menanggung tegangan lebih panjang dalam rantau plastik. Dapatan juga menunjukkan yang jurang jalur bagi kedua helaian s-triazina dan heptazina meningkat berfungsikan terikan tegangan dwipaksi. Sifat elektronik bagi kedua-dua helaian heptazina dan s-triazina di bawah medan elektrik hingga nilai maksimum 8 V/nm kekal tak berubah. Bagi sistem-sistem Mn-, dan Fe- terbenam heptazina ($C_6N_7 - Mn$ dan $C_6N_7 - Fe$) dan s-triazina ($Mn - C_6N_6$ dan $Fe - C_6N_6$), pendekatan DFT+ U telah digunakan (Yang mana, $C_6N_7 - Mn$, $C_6N_7 - Fe$ dan $Mn - C_6N_6$, $Fe - C_6N_6$ keseluruhannya dirujuk sebagai $C_6N_7 - TM$ dan $TM - C_6N_6$ masing-masing). Kesemua sistem didapati stabil secara struktur dan mekanik. Keputusan menunjukkan tenaga pengikatan sistem boleh dimodulasi dibawah aruhan terikan tegangan dwipaksi dan medan elektrik seranjang. Momen magnet bagi sistem $C_6N_7 - TM$ dan $TM - C_6N_6$ ini di bawah terikan mekanik, medan elektrik kekal tidak berubah. Ini menunjukkan dari $C_6N_7 - Mn$ ke $Mn - C_6N_6$, terikan tegangan dwipaksi meningkatkan jurang jalur sistem ini, manakala sifat elektronik logam dan separa logam muncul bagi kes-kes $C_6N_7 - Fe$ dan $Fe - C_6N_6$ masing-masing. Tambahan pula, sifat-sifat struktur, elektronik, dan magnet bagi $C_6N_7 - TM$ dan $TM - C_6N_6$ beserta atom-atom dan molekul-molekul terjepap juga turut disiasat menggunakan pendekatan DFT+ U . Dapatan menunjukkan yang atom-atom (C, N, O, H) dan molekul-molekul (CH_4 , N_2 , O_2 , H_2 , CO, CO_2) terjepap kimia pada kedua-dua sistem $C_6N_7 - TM$ dan $TM - C_6N_6$. Penjerapan adatom menghasilkan pelenturan dalam sistem $C_6N_7 - TM$ tersebut. Ditemui, pada sesetengah kes, sifat semikonduktor bagi sistem $C_6N_7 - Mn$ dan $Mn - C_6N_6$ dan sifat logam/separa logam bagi $C_6N_7 - Fe/Fe - C_6N_6$ dapat dimodulasikan kepada logam, separa logam dan semikonduktor masing-masing. Jumlah momen magnet sistem $C_6N_7 - TM$ dan $TM - C_6N_6$ berserta

atom-atom dan molekul-molekul terjerap berkurang/bertambah, bergantung kepada gandingan magnet bagi elektron tak berpasangan dalam petala 3d atom Mn atau Fe serta atom-atom/molekul-molekul terjerap.

**AB-INITIO INVESTIGATION OF STRUCTURAL, ELECTRONIC, AND
ADSORPTION PROPERTIES OF GRAPHITIC CARBON NITRIDE SHEET
WITH EMBEDDED TRANSITION METAL Mn AND Fe ATOMS**

ABSTRACT

At present, research interest in magnetic nanostructures are directed towards the search for suitable substrates for transition metal (TM) atoms embedment. The appropriate substrate is expected to preserve its intrinsic properties and that of bound TM atoms. Graphene and related surfaces with uniformly compacted hexagonal rings have been a frequent choice for trapping TM atoms due to their desirable surface properties. However, reports have shown that the TM atoms diffuse easily on these 2D surfaces as a result of low adsorption energies. To ensure the immobility of the TM atoms on the surface, much efforts have been made to synthesise 2D materials with inherently regular cavities e.g, carbon nitride (CN). Intensive physical properties investigations have been carried on pure and doped graphitic CN sheet over the past few years. However, the physical properties of pure and doped CN under external perturbations remains elusive. By applying first-principles method based on density functional theory (DFT) with the aid of QUANTUM ESPRESSO package, the ground state physical properties of both pure and TM-embedded in the heptazine and s-triazine sheets under mechanical strain, electric field and chemical adsorption have been investigated. Results show that the heptazine and s-triazine sheets are structurally and mechanically stable. The calculated values of the critical strains (proportionality and yielding points) indicates that s-triazine sheet can withstand larger tension in linear elastic region more than heptazine sheet and both sheets can withstand longer tensions

in the plastic region. Findings also show that the bandgap of both s-triazine and heptazine sheets increases as a function of bi-axial tensile strain. The electronic properties of both heptazine and s-triazine sheets under electric field up to a maximum value of 8 V/nm remain unchanged. For the Mn-, and Fe- embedded heptazine ($C_6N_7 - Mn$ and $C_6N_7 - Fe$) s-triazine ($Mn - C_6N_6$ and $Fe - C_6N_6$) systems, DFT+*U* approach was used (Herein, $C_6N_7 - Mn$, $C_6N_7 - Fe$ and $Mn - C_6N_6$, $Fe - C_6N_6$ collectively refer to as $C_6N_7 - TM$ and $TM - C_6N_6$ respectively). All systems have been found to be structurally and mechanically stable. Results show that the binding energy of $C_6N_7 - TM$ and $TM - C_6N_6$ systems can be modulated under the influence of bi-axial tensile strain and perpendicular electric field. The magnetic moments of $C_6N_7 - TM$ and $TM - C_6N_6$ systems under mechanical strain, electric field remain unchanged. It is shown that from $C_6N_7 - Mn$ to $Mn - C_6N_6$ the bi-axial tensile strain increases the band gap of these systems, while metallic and half-metallic electronic characters appeared in the cases of $C_6N_7 - Fe$ and $Fe - C_6N_6$ respectively. The structural, electronic and magnetic properties of $C_6N_7 - TM$ and $TM - C_6N_6$ with adsorbed atoms and molecules have been investigated using a DFT+*U* approach. The findings show that the atoms (C, N, O, H) and molecules (CH_4 , N_2 , O_2 , H_2 , CO , CO_2) chemisorbed on both $C_6N_7 - TM$ and $TM - C_6N_6$ systems. Adsorption of adatoms results in buckling in the $C_6N_7 - TM$ system. It is found that, in some cases, the semiconducting property of $C_6N_7 - Mn$ and $Mn - C_6N_6$ and metallic/half-metallic property of $C_6N_7 - Fe/Fe - C_6N_6$ systems can be modulated into metallic, half-metallic and semiconducting, respectively. The total magnetic moment of the $C_6N_7 - TM$ and $TM - C_6N_6$ systems with adsorbed atoms and molecules reduced/increased, depending on the magnetic coupling of the unpaired electrons in the 3d orbitals of Mn or Fe atom and the adsorbed atom/molecules.

CHAPTER 1

INTRODUCTION

1.0 Motivation

The clusters of transition metal (TM) have been an interesting topic for both fundamental and applied research as a result of the progress towards downsizing the solid to atom. The central interest in the TM cluster investigation is rooted from its high surface-to-volume ratio manifested by reduced coordination number of the surface atoms in the clusters. Currently, the investigation of exotic physics associated with the TM cluster in condensed phase has been concentrated on revealing the physical and chemical properties of their corresponding atoms under different conditions [1-3]. Understanding these properties is essential for identifying and designing material based on TM cluster for wider potential nanoscale applications.

As a strategy, to design a multifunctional material based on TM cluster one first checks the nature of the TM cluster itself, and later introduce some deliberate perturbations such as being embedded to a nanosheet. Preference must be given to nanosheets that will preserve their intrinsic property and that of the TM cluster. For tailoring the properties of a TM cluster in the advanced magnetic material application, two important points must be taken into consideration. First, the TM atoms should have a ferromagnetic spin state, to begin with so that their magnetic moment can be subsequently maximized. Second, the magnetic anisotropy of the cluster should be larger in order to preserve the orientation of such spin state and its possible interaction with the spin of a ferromagnetic electrode.

For the photocatalytic application, TM cluster-based materials should be a semiconductor which responses optically to in the visible light region. Additionally, such TM clusters should display large reactivity in those catalytic processes which

they are designed for. This enhanced chemical tendency can be maximized if the cluster size is reduced to atomic level.

Isolated diatomic TM clusters can be classified into homonuclear or heteronuclear type, depending on the chemical composition of the TM atoms. Variation in the composition of the TM cluster results in significant modulation to the chemical reactivity and electronic structure of the clusters. However, in most cases, the physical properties of these clusters may vary non-monotonically. For example, the spin-polarised first-principles calculations as reported in Ref. [5] have shown that the total magnetic moment of the CoX_n clusters increases as a function of species X, where $X = \text{Fe, Co, or Ni}$, and $n = 1 \text{ or } 2$. Conversely, the FeX_n -clusters do not show any definite trend in the computed magnetic moment. This implies that the Fe atom couples either ferromagnetically or antiferromagnetically with the neighboring atoms in the FeX_n clusters. As a result of the coupling, the total magnetic moment of the FeX_n clusters becomes increased or decreased [5]. The reported findings have also been confirmed by Gutsev *et al.* [6].

Developing TM complexes with a well-defined magnetic moment presents a research challenge. One of the approaches is through investigating the effects when these TM clusters are bound on a metallic support. The reason being that metallic support might have favorable chemical sensitivity with the atoms of the condensed clusters [1]. Unfortunately, owing to the enhanced reactivity between the bound TM clusters and the surrounding atoms of the support material which hampers the ordered ferromagnetic spin configuration of the TM atom, the issue has not been resolved yet. Incontestably, the monotonic magnetic moment can be achieved if the atoms in the cluster are regularly separated on an inert surface. Among these inert surfaces, carbon and related sheets have been the most preferred [3, 7]. These sheets have been

demonstrated as good support materials for potential applications in spintronics and catalysis [2, 8].

The recent interest in advanced magnetic application has been the search for material with well-ordered magnetization for usage in high data storage devices. The target is to produce one-bit storage with a single atom. After a successful isolation of hexagonal monolayer structure called graphene [9], there has been a remarkable interest in the investigations of the physical properties of TM adatoms and dimers on two-dimensional (2D) hexagonal surfaces [2, 3, 7]. The expectation is that the chemically inert surface will preserve the intrinsic properties of both the bound TM nanostructures and the host surfaces. However, the main challenge with the uniformly compacted hexagonal 2D surfaces is that the TM atoms are not anchored firmly on these surfaces [10, 11]. This could result in the formation of bigger clusters that are vulnerable to the reduction of the previously mentioned exotic properties. Moreover, the thermal instability (low Curie or Neel temperature) as a result reduced TM cluster size is also a challenge. This could also yield a low magnetization of TM clusters after switching off the applied magnetic field.

To address these challenges which hinder their full explorations in catalysis and spintronic fields, more research efforts have been made to synthesize 2D materials with naturally well-defined cavities [12]. Among the recently synthesized porous 2D materials, carbon nitride (CN) nanostructures [13] has received tremendous attention for both theoretical and experimental investigations [14-16]. This is due to its intrinsic chemical inertness, thermal and mechanical stabilities, in addition to its environmental friendliness. The band gap range (~ 2.7 eV) [17] which is good for harnessing the visible region of solar spectrum has further qualified the porous CN nanostructure for photocatalysis as compared to TiO_2 .

By introducing magnetic nanostructures into its well-ordered porous sites, it can be tailored as a diluted magnetic semiconductor [18, 19]. The embedded TM nanostructure can also serve as a stabilizer to avoid the formation of diatomic nitrogen within the porous site which are vulnerable to the destruction of the hexagonal structure [20]. An intriguing question to ask is if porous CN sheet with embedded TM atom system could have enhanced physical properties as a multifunctional material for both magnetic and catalytic applications under the influence of external perturbations such as mechanical strain, electric field and adsorptions of atoms and molecules. To the best of our knowledge, these effects of external perturbations on ground state properties of pure and TM atom embedded CN sheet have not been studied experimentally, and theoretically until now.

Therefore, this research work seeks to answer the questions by theoretically and computationally predicting the stability, electronic and magnetic properties of porous CN sheet with embedded Mn and Fe atoms systems under the influence of external perturbations. Specifically, Mn and Fe atoms have been considered due to their abundance and the open shell configurations of $3d^5$ orbital of Mn atom and $3d^6$ orbital of Fe atom made their spin magnetic moment larger compared to the remaining 3d TM atoms. Density functional theory (DFT) as the best computational tool for dealing with topics, such as material stability, surface science, semiconductor and magnetism would be employed. However, DFT alone is not sufficient for predicting the ground state properties of strongly localized states involving transition metals. This limitation has been addressed by describing the localized states with an independent Hubbard model of electron interacting an effective screened Coulomb potential, U . It is hope that the future experimental work on the ground state properties of the studied system would commensurate with our theoretical predictions.

1.1 Pure Graphitic Carbon Nitride Sheet

CN nanostructure belongs to a group with a common chemical formula C_xN_y , where x and y represent the number of C and N atoms in the unit cell. It was long ago reported as a super hard material in the form of beta - C_3N_4 by Liu and Cohen [21]. The study that formulated the remaining five members of the group was done in 1996 by Teter and Hemley [22]. They are; alpha - C_3N_4 , beta - C_3N_4 , cubic - C_3N_4 , pseudocubic - C_3N_4 and graphitic - C_3N_4 (see Fig. 1.1 (a)-(d)). The readily available heterocyclic building blocks in the form of melamine, cyanamide, and dicyandiamide have made CN sheet one of the cheapest 2D materials to synthesize using various techniques [23, 24]. According to the theoretical predictions, the allotropes of graphitic C_3N_4 (g - C_3N_4) which are known as heptazine and s-triazine sheets are among the most stable under ambient conditions [22, 25] (See Fig 1.1 (e)). As a building block of all the allotropes, g - C_3N_4 is a wide band gap semiconductor and had been synthesized in a single layer like that of graphite [13, 26].

According to the heterocyclic building block of g - C_3N_4 two common derivatives can be deduced: single triazine-based (g - s - C_3N_4) and tri-single triazine-based g - t - C_3N_4 (known as heptazine) [26, 27]. As depicted in Fig 1.1 (e) Left, the hexagonal structure in the unit cell of heptazine is compacted side by side. s-triazine (chemical formula: g - C_6N_6) which is another derivative of graphitic C_xN_y has two of its hexagonal rings (g - C_3N_3) connected via C - C bond [14]. The derivative of graphitic C_xN_y can have different electronic properties ranging from semiconducting to half-metallic depending on the C and N atomic coverage in their hexagonal structure and unit cell. For example, a half-metallic electronic behavior with the ferromagnetic ground state [28] has been reported for a triazine-based derivative of g - C_4N_3

whereas the rest of the derivatives are non-magnetic with wide or small band gaps [17, 29, 30].

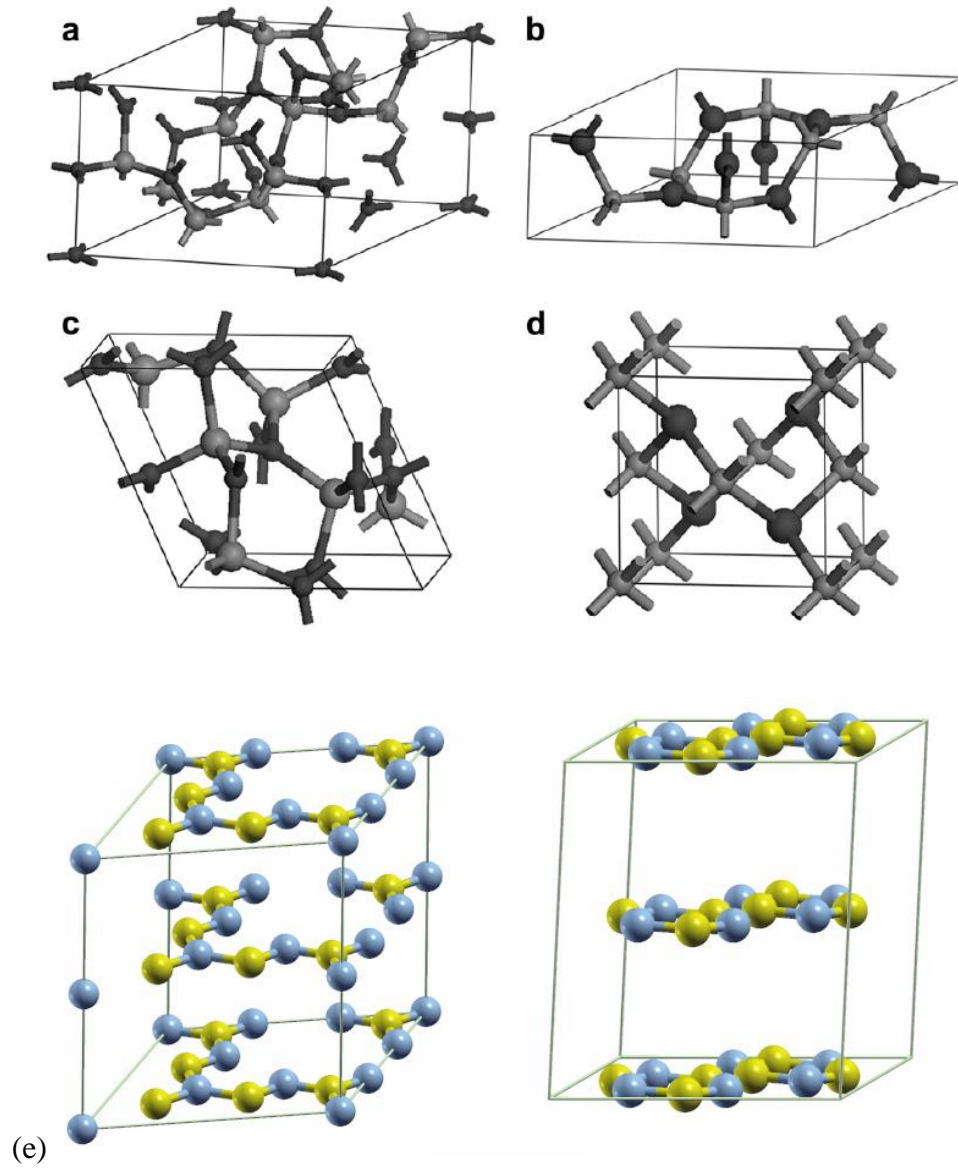


Figure. 1.1 Primitive cells of 4-dense C_3N_4 phases: (a) $\alpha - C_3N_4$, (b) $\beta - C_3N_4$, (c) cubic $- C_3N_4$ and (d) pseudocubic $- C_3N_4$. Carbon and nitrogen atoms are depicted in big and small balls respectively[17]. (e) graphitic $- C_3N_4$.

Recent theoretical studies on graphitic CN sheets have been mainly focused on tailoring the physical properties of graphitic CN sheet when nanostructures are embedded on its surface [18, 19]. This is due to its inherent well-dispersed porous sites

which are good for anchoring nanostructures at even dispersions as well for its intrinsic remarkable properties for modern nanoscale applications. However, less attention is paid to study the ground state properties of the pure CN sheet and the responses on the electronic properties under the external perturbations, such as mechanical strain and electric field.

Due to a direct relationship between structural features and the electronic properties of materials, strain response has been widely used as an effective way to modulate material properties. For example, the band gap of graphene monoxide sheet has been found to be modulated under the influence of external strain [31]. Moreover, strain engineering has been used experimentally for controllable thin film growth and device fabrication, which usually results in variation of materials properties [32-34]. These previous works on similar 2D material could serve as a hint to understand the effects of these external responses on $g - C_xN_y$ nanosheets.

Molecular dynamic simulations have been used recently to demonstrate the remarkable mechanical property and thermal conductivity of CN thin films [35]. It was found that heptazine is mechanically stable at a maximum of 600 K and exhibit fewer fractures under larger tensions. The fracture pattern under larger tensions has also been reported to depend on the chemical bonds, density values, topologies and stretching directions [35]. On the other hand, one of the best approaches for computation of mechanical properties of nanomaterials that can be directly compared against experimental results is via the *ab-initio* method based on density functional theory (DFT).

Using DFT calculation, Li [36] have found a new method of bulk modulus estimation through chemical disordering in silicon carbide. Qin *et al.* [37] reported that the Poisson's ratio and robustness of silicene depend largely on uni-axial strains.

Furthermore, the band gap of the silicene nanosheet remains unperturbed under uni-axial strain. The nonvariant band gap observed is related to the sp^2/sp^3 interplay in the silicene structure [37]. While Liu *et al.* have reported electronic and magnetic property modulations of graphitic triazine-based CN ($g - C_3N_4$) under uni-axial tensile strain [38].

Nonetheless, first-principles calculations based on DFT of in-plane stiffness, elasticity, and responses on electronic property under symmetric deformation and applied perpendicular electric field is still lacking. There has been a report on the mechanical stability of $g - t - C_4N_3$ sheet in the light of phonon dispersion using density functional perturbation theory (DFPT) approach [39]. The $g - t - C_4N_3$ sheet which is a C - doped heptazine, and the $g - t - C_4N_3$ sheet is one of the derivatives of $g - C_3N_4$ [39]. It was found that the phonon spectrum and phonon frequency density of state show no imaginary phonon mode. The $g - t - C_4N_3$ sheet was also found to be stable under strain up to a few percent (0 – 5%). It is hence logical to investigate the mechanical and electronic properties and of heptazine and s-triazine sheet using the first-principles framework.

1.2 Transition Metal Embedded Graphitic Carbon Nitride Sheet

Many researchers have engaged in the search for suitable 2D substrates that anchored TM atoms firmly for both fundamental and applied types of research [40, 41]. The appropriate substrate is expected to preserve its intrinsic properties and that of bound TM atoms. 2D carbon-based and related surfaces with compacted hexagonal rings have been the most frequent choice for trapping TM atoms [42, 43]. This is due to their wide surface area. Numerous works have been done to investigate the stable geometries and electronic properties of TM atoms adsorption on graphene and boron nitride sheets [42, 44].

The major drawback in these systems is the lack of inherent cavities to firmly accommodate foreign nanostructures within its surface. Moreover, the large surface free energy of the TM atoms would make them accumulate easily to form cluster on these sheets. To prevent the diffusion of the bound TM nanostructures on the hexagonal 2D surfaces, various defects sites have been proposed [45, 46]. Formation of defects sites would presumably have anchored the TM atoms on surfaces. However, having a regular defect on surfaces at atomic-scale might lead to ambiguous results experimentally at low coverage. On this note, more research efforts have been employed to synthesis 2D materials with inherently and uniformly arranged cavities [46]. Among the recently synthesized porous 2D materials, graphitic CN sheet has been the most widely investigated for both fundamental and applied types of research. This is due to its fantastic chemical and physical properties as a right candidate for many potential applications such as hydrogen production from water and bioimaging medical application [15, 16, 47].

To tailor the properties of porous CN sheet for advanced magnetic material such as diluted magnetic semiconductor, theoretical [18, 40, 48] and experimental [8, 49] investigations on graphitic CN sheet with embedded single atoms have been carried out. Du *et al.* theoretically reported ferromagnetic ground state with half-metallicity by uniformly substituting N atom with C atom to form C – doped triazine-based g – C_4N_3 [28]. Additionally, evidence of ferromagnetic ground state at ambient conditions by adsorption of hydrogen dangling bonds at some favorable sites on heptazine monolayer has been reported [50]. However, producing a stable spin ordering upon doping of non-magnetic atoms into the CN sheet remain unclear. It is hence reasonable to examine whether g – C_3N_4 can endure ferromagnetic ground state by the traditional method of incorporating TM atoms into its free-standing form.

The geometric, electronic and magnetic properties of $g-t-C_3N_4$ with embedded B, Al, and Cu atoms systems have been theoretically investigated [51]. It was found that Cu atoms are energetically stable when located above the center of the triazine ring. Moreover, the report shows that interstitial sites doping produces thermodynamically stable non-planar structures. Cu-doped triazine system yields a total magnetic moment of $1.0 \mu_B$ which is mainly localized around p_z like-orbitals of the sheet. A half-metallic electronic character with anti-ferromagnetic ground state is found for Cu-doped triazine systems in both DFT calculations with a generalized gradient approximation (GGA) of Perdew-Burke-Ernzerhof (PBE) functional and Heyd-Scuseria-Ernzerhof (HSE) hybrid functional. Curie temperature was not calculated for Cu-doped triazine system due to the fact that long-range magnetic ordering is usually found in the system with the ferromagnetic order at zero temperature.

Ghosh *et al.* studied the geometric, energetic, electronic, magnetic and optical properties of 3d TM atoms embedded $g-t-C_3N_4$ systems [18]. It was found that embedded TM atoms are energetically more stable when situated at the porous sites of $g-t-C_3N_4$ sheets. Their results show that in the systems the semiconducting character of $g-t-C_3N_4$ is modulated into metallic after TM (including Cu) embedment in the cavity. The d orbitals of TMs hybridize with the π -orbitals of the $g-t-C_3N_4$ sheet and the TM-embedded $g-C_3N_4$ (TM- $g-C_3N_4$) system become metallic. The magnetic moment of the embedded 3d TM atoms is comparable to their isolated values in most cases. However, Mn atoms couple antiferromagnetically whereas Cu and Zn atoms are nonmagnetic in the ground state of their corresponding TM- $g-C_3N_4$ systems [18].

The claims for magnetic ordering in Mn, Cu embedded $g-t-C_3N_4$ sheets and

metallic behavior for Cu embedded system at relatively the same separations are in contrast to what was observed by Zhang *et al.* [40] and Meng *et al.* [51] in the same allotropes. In a similar allotrope, Du *et al.* [52] suggested that Mn and Cu atom embedded in C_2N monolayers possess ferromagnetic and paramagnetic ground state respectively when the TM atoms are close to each other, while Meng *et al.* [51] observed antiferromagnetic ground state with the half-metallic electronic character for Cu – doped triazine system.

Overall, the claim for the magnetic ordering of TM atoms embedded in CN remains unclear. However, it is feasible to have negligible interactions between neighboring images of TM atoms if the embedded TM atoms are spatially well separated apart in the cavity. The effort to clarify the magnetic ordering issue hence could become less complicated.

More recently, Choudhuri *et al.* [19] performed first-principle calculations based on density functional theory on another allotrope of the carbon-nitride monolayer (g – t – C_3N_4) with embedded 3d transition metal atoms (TM – g – C_3N_4) systems. Their results show that the g – t – C_3N_4 with embedded Cr, Mn, and Fe systems are dynamical, thermally and mechanically stable. Moreover, their calculation predicts high-temperature ferromagnetism and high magnetic anisotropy energy (MAE) for Mn and Fe embedded g – t – C_3N_4 systems with a peak value per atom occurring in Cr@g – t – C_3N_4 Cr. Their results for the ferromagnetic ordering of Mn atom in similar graphitic CN sheet under ambient conditions support the reported findings by Du *et al.* [52]. Choudhuri *et al.* [19] further reported an enhanced MAE in the presence of an external electric field, an amount far more than the value computed without an electric field.

It is also reported that the semiconducting character of the CN with embedded 3d TM in most cases of the calculations mentioned above is modulated into metallic character because of dispersed TM atoms embedment in the cavity of the $g-t-C_xN_y$ sheet [18, 19]. Therefore, recovering the $g-t-C_xN_y$ intrinsic band gap while preserving the induced magnetism by the embedded TM atoms presents a new research challenge. External perturbations such as electric field, [53] mechanical strain [54, 55] and chemical functionalization [43] are commonly employed for controlling monolayers physical properties. This is because the applications of these external fields would presumably result in strong/weak interactions between the embedded nanostructures and the surrounding atoms.

A theoretical approach based on DFT has proved that molybdenum disulfide (MoS_2) monolayer under small deformations would render the band gap to become smaller. As a result, the semiconducting MoS_2 monolayer exhibits metal electronic character at 8% deformation [55]. In the Fe-doped molybdenum disulfide (Fe- MoS_2) sheet, the magnetic moment was reported to change from 2.04 to $4 \mu_B$ when the bi-axial tensile strain reached 3.5% [54]. Another report shows that electronic properties, such as magnetic semiconductor and spin-gapless semiconductor can be achieved in Fe- MoS_2 system by the applied strain [54]. Experimentally, tensile strain is needed for CN sheet deposition on a substrate. The straining process of the sheet during the growth/deposition would result in material's properties modulations [32].

Besides advanced magnetic applications, CN with embedded TM systems can also be tailored for heterogeneous catalysis and as a membrane for gases purifications [56-58]. For example, single atomic catalyst (SAC) is one of the cheapest and easiest ways of achieving efficient catalysis. To date, many monolayer sheets have been theoretically and experimentally tested for heterogeneous catalysis. Boron nitride [59],

graphene [60], graphyne [61], silicene [43] have been the most frequent choice. This is due to their large conductivities, thermal stability, and large surface area. Ab-initio calculations based on DFT have demonstrated that graphene with embedded Au, Fe, and Pt [60, 62, 63] atoms produced good catalytic activity for CO oxidation and oxygen reduction. Experimentally, favorable catalytic activities have been confirmed for graphene with supported single Pd and Pt using deposition method [64, 65].

Although good catalytic activity has been confirmed for SACs of carbon and related monolayers with 3d TM atoms, the adsorption/binding energies of 3d TM atoms on their surfaces are usually weak and could result in nucleation of atoms that renders reduction in catalytic activity. Monolayer porous carbon sheets embedded with TM atoms [48] are desirable for SACs [58] and gases purification [56]. This is due to their intrinsically regularly array of porous sites. These porous sites are strongly anchored to 3d TM while maintaining almost planar structure and the intrinsic physical properties of the sheets [48]. A current study along this direction has supported the theoretical assertion of synthesizing high-quality SACs using porous 2D materials with well-dispersed 3d TM atoms. Due to the strong binding of 3d TM atoms on the C_2N sheet, the well-dispersed atoms in the porous sites are not prone to the cluster formation [58]. Moreover, the intrinsic physical properties of both C_2N sheet and the 3d TM atoms are maintained [52].

This thesis undertakes a theoretical study of stable geometries, mechanical, electronic and magnetic properties of TM-embedded graphitic systems under the influence of mechanical strain and the electric field. To be specific, Fe- and Mn-embedded heptazine and s-triazine sheets have been studied. Additionally, chemical functionalization with different types of atoms (C, N, O, H atoms) and (biogas

products) molecules (CH_4 , N_2 , O_2 , H_2 , CO , CO_2) adsorbed onto Fe-, and Mn-embedded heptazine and s-triazine systems have been considered.

Heptazine and s-triazine sheets have common electronic property and possess a well separated porous site which will ensure no interactions between the embedded TM atoms. Mn and Fe are chosen instead of other 3d TM species due to its well-ordered spin configurations in the d orbital and desirable characteristics for spintronic and SAC applications. Another factor is the doping strain provided by the Mn, and Fe atoms in the cavity which ensures a relative stability of the C – C and C – N bonds in the hexagonal ring. The investigation involves the calculations of ground state physical properties of pure heptazine and s-triazine sheets under external perturbation as a benchmark to help understand the subsequent heptazine and s-triazine with embedded Mn, and Fe systems.

1.3 Research objectives

This study embarks on the following objectives:

- 1) To determine the structural and mechanical properties of pristine heptazine and s-triazine sheets based on formation energy, bond length, charge density distributions and elastic constants.
- 2) To analyze the electronic properties of the pristine heptazine and s-triazine sheets under the influence of external perturbations based on a total and projected densities of states and band structures.
- 3) To determine the structural and mechanical properties of Fe- and Mn-embedded heptazine and s-triazine systems based on the binding energy, bond length, charge density distributions and elastic constants.
- 4) To examine the magnetic and electronic properties of the Fe- and Mn-embedded heptazine and s-triazine systems under the influence of external

perturbations based on magnetic moment, total and projected densities of states and band structures.

- 5) To investigate the structural, magnetic and electronic properties of Fe- and Mn -embedded heptazine and s-triazine systems with adsorbed atoms (C, N, O, H atoms) and molecules (CH_4 , N_2 , O_2 , H_2 , CO , CO_2).

1.4 Scope and Limitation

This thesis is limited to the study of ground state physical properties of pure and doped heptazine and s-triazine sheets under external perturbation with the aid of density functional theory calculations. Although there are number of studies for the transition metal embedded carbon nitride (TM-CN) sheet. There are however, no studies on the investigation of the effect of mechanical strains, electric field and adsorption of atoms/molecules on the structural, electronic and magnetic properties of TM-CN sheet. This thesis is an attempt to fill in the gap. There are number of limitations related to the DFT calculations for the studied systems. These problems are mainly associated to the treatment of electron exchange and correlation effect for a strongly localized state involving transition metals (TM) and the adsorption properties. For the cases of Mn, and Fe atom in the studied material, the limitation has been addressed by describing the localized states with an independent Hubbard model of electron interacting an effective screened Coulomb potential, U . Dispersion forces have not been considered for adsorption properties of TM-embedded heptazine, and s-triazine with adsorbed atoms/molecules complexes. The van der Waals (vdW) interactions are not expected to play role where strong chemical bonds are formed. However, in some cases where the adsorption energies are relatively low, dispersion forces could be relevant.

1.5 Thesis outline

The contents are organized as follows:

Chapter 1: introduces the research motivation and review of relevant works. It also presents the research aims and objectives and organization of thesis. Chapter 2: reviews the electronic structure calculation methods. Specifically, the discussion covers the basic concepts of density functional theory starting from Hohenberg-Kohn theory [66] and Kohn-Sham [4]. The functional forms of the exchange and correlation in the local density approximation [67] and the generalized gradient approximation [68] are presented. Lastly, the plane wave basis set in QUANTUM ESPRESSO code [69] are discussed. It also discusses the methodological details and models used in the research. Moreover, the chapter presents the preliminary calculations as a bench mark for the general calculations. Chapter 3: presents the results and discussions for heptazine and s-triazine sheets. Chapter 4: presents the results and discussions for Fe- and Mn-embedded s-triazine systems with adsorbed atoms and molecules. Chapter 5: presents the results and discussions for Fe- and Mn-embedded s-triazine systems with adsorbed atoms and molecules. Chapter 6: summarizes the results obtained and possible future outlook.

CHAPTER 2

THEORETICAL FRAMEWORK AND METHODOLOGY

2.0 Introduction

In this chapter, an overview of the theoretical background, the approximations used in this study will be presented. The exchange-correlation functional and the atomic pseudopotential formalism will be briefly introduced. The implementation of Bloch's theorem which is based on periodic crystal lattices will be described. Afterwards, the chapter briefly presents the QUANTUM ESPRESSO code, and the types of calculations associated with the code. Finally, the rest of the subsections discuss the computational procedure and preliminary calculations to bench mark the computational accuracies of the systems considered.

2.1 Electronic Structure Calculations

Numerical methods provide an approximate alternative for describing physical and chemical quantities of real materials. These approximate concepts are based on the quantum mechanical approach. To describe the behavior of the constituent particles in the system quantum mechanically, a full many-body Hamiltonian must be known. For a many-body system of electrons and nuclei, the Hamiltonian is given by

$$\hat{H} = -\hbar^2 \sum_i \frac{\nabla_p^2}{2m_e} - \hbar^2 \sum_p \frac{\nabla_p^2}{2m_p} + \frac{1}{2} \sum_{i \neq j} \frac{e^2}{|r_i - r_j|} - \sum_{i,j} \frac{z_p e^2}{|r_i - R_p|} + \frac{1}{2} \sum_{p \neq q} \frac{z_p z_q e^2}{|R_p - R_q|}, \quad (2.1)$$

where r_i , m_e is the position and mass of the i -th electrons; z_p , m_p and R_p are the charge, mass and position of the p -th nucleus respectively. The first and second terms define the kinetic energies of electron and nuclei, while the last three terms describe the potential energy of the electron-electron, electron-nuclei, and nuclei-nuclei columbic interactions respectively. For a very simple system, the solution of the Hamiltonian equation (2.1) (time-independent and without relativistic effect) can

describe the physical properties associated with the system. However, it is numerically difficult to obtain an exact solution for a system comprising many interacting electrons. Thus, many interacting electrons systems require next level of approximation methods to simplify the many-body Schrödinger equation.

The starting approach to tackle this problem is to separate the interacting electrons into core and valence electrons. This is obviously possible by looking at the Hamiltonian in the equation (2.1) (above), where p, q and i indices represent core ions and the valence electrons respectively. The next approximation to many-body Schrödinger equation is called Born-Oppenheimer (BO) adiabatic approximation [70]. This approximation ignores the degree of freedom associated with the motion of nuclei and electrons in addition to their wave function for the total energy calculations. In their estimations, the nuclei being the heaviest in terms of their masses are at rest relative to the electronic motion. Consequently, the dynamics of the electrons and nuclei (treated classically) is decoupled. The associated wave function can be decoupled into a product of electronic and nuclear components as

$$\psi(r, R) = \psi_e(r, R) \times \psi_n(r). \quad (2.2)$$

The ion-ion interaction term cannot be ignored because their position is significant in getting the minimum energy of the system. Using Hartree atomic units ($\hbar = m_e = e = 1$) notation, the many-body Hamiltonian for the system reduces to

$$\hat{H} = \hat{T}_{\text{elec}} + \hat{V}_{\text{ion-elec}} + \hat{V}_{\text{elec-elec}} + \hat{V}_{\text{ion-ion}}, \quad (2.3)$$

with each term maintaining its usual definition. Although the reduced Hamiltonian equation (2.3) captures all the significant terms needed for quantum mechanical properties of the system, it is still too expensive to solve. To overcome the problem, there is need for more approximations.

2.1.1 Independent-electron Approximation

Even though Born-Oppenheimer approximation has successfully decoupled the Hamiltonian into a sum of the electronic and nuclear parts, it does have limitations for treating the effects of many particles interaction in the system. This limitation makes the electronic problem even more complicated to be solved. To overcome this limitation, further approximation named Independent-electron method has been proposed. This method tries to account for the complicated electron-electron interaction by adopting a periodic potential $V(r)$ defined in the single electron Schrödinger equation as

$$\left(\hat{T}_{\text{elec}} + \hat{V}(r)\right)\psi_k(r) = \varepsilon(k)\psi_k(r), \quad (2.4)$$

where the index k represents a wave vector and r is the position of the electron.

In practical, equation (2.4) provides an approximate approach to solve many-electrons system since periodicity is accounted for in the system. However, the complications which are unavoidable in the approximation is that the potential $V(r)$ describing the interactions must be known. This limitation will require more mathematical techniques. Hence necessitates more approximation methods. In all cases, the developed methods have their advantages and shortcomings. The next level of approximation method that provides an improvement to the solution of the many-electrons problem from the previous approaches is called Hartree (H) approximation [71]. The H approximation method was able to decouple the periodic potential $V(r)$ into sum up electronic and ionic parts. Hartree assumes that one electron feels the electric field of the other electrons and treated the rest of the electrons as a uniform distribution of negative charges with charge density expressed as

$$n(r)_i = -e \sum_i |\psi_i(r)|^2 \quad (2.5)$$

The index i in equation (2.5) shows that the electrons obey Pauli Exclusion Principle.

Thus, the electron potential can be defined in terms of charge density as follows:

$$V_{\text{elec}} = e^2 \sum_i \int |\psi_i(r')|^2 \frac{1}{|r-r'|} dr'. \quad (2.6)$$

So that potential $V(r)$ becomes

$$\hat{V}(r) = \hat{V}_{\text{ion}}(r) + \hat{V}_{\text{elec}}(r). \quad (2.7)$$

By substituting equation (2.7) into equation (2.4). The Hartree equation reduces to

$$[\hat{T}_{\text{elec}} + \hat{V}(r)]\psi_i(r) = [\hat{T}_{\text{elec}} + \hat{V}_{\text{ion}}(r) + \hat{V}_{\text{elec}}(r)]\psi_i(r). \quad (2.8)$$

Yet in spite of the recorded success, the Hartree method suffers some limitations. The effects of anti-symmetrization of many-electrons wave functions, and the correlations of many electron interactions are neglected. On this note, taken into considerations of these effects into the Hartree approximation requires rigorous numerical approximations. Next is the Hartree-Fock approximation [69] which is yet another wave function method but considers exchange term in the Hartree equation (2.8).

2.1.2 Hatree-Fock Approximation

Within the Hartree-Fock (HF) approximation, the starting point is to include explicitly the anti-symmetric property of the electronic wave function into the independent electron approximation. The term added is responsible for the exchange term. This is important because electrons are fermions and hence obey Pauli exclusion. Considering an N-electron system, the solution of the time-independent Schrödinger equation can be achieved by substituting the wave function $\psi(r)$ by a Slater determinant [72] of single-electron wave functions expressed as

$$\psi(x_1, x_2, x_3, \dots) = \frac{1}{\sqrt{N!}} \text{Det}[\psi(x_1), \psi(x_2), \dots \psi(x_N)]. \quad (2.9)$$

In the Slater determinant, the anti-symmetric requirement of electrons is satisfied. This provides an easy scheme to express an exchange term acting between the electrons of the same spin given by

$$V_j^{\text{exchange}} = -\frac{1}{2} \sum_j \int \psi_j^*(r') \psi_i(r') \frac{1}{|r-r'|} \psi_j(r) d^3r'. \quad (2.10)$$

By putting equation (2.10) into the Hatree approximation equation (2.8), gives the Hatree-Fock approximation equation (2.11).

$$\varepsilon_i \psi_i(r) = [\hat{T}_{\text{elec}} + \hat{V}_{\text{ion}}(r) + \hat{V}_{\text{elec}}(r)] \psi_i(r) + V_j^{\text{exchange}}. \quad (2.11)$$

Thus, the HF method has been proved to be successful in addressing problems involving adsorption [73] and defects in solids [74] because of the self-consistent approach in dealing with exchange term.

However, it suffers yet another limitation due to its failure to account for coulomb repulsion of the electrons which is responsible for the correlation of the electrons [75]. Consequently, the approximation cannot be used to describe the properties of a metallic material like the density of states because electron velocity around Fermi level have infinite value according to HF method.

2.1.3 Density Functional Theory

While HF approximation has been known to be successful for treating electronic structure problem via many-electron wave functions for small systems, it doesn't capture the solutions of larger systems. This is so due to the increase in numerical complications as the number of correlated electrons increases. For example, for an N-electrons system, the wave function required to treat instantaneous coordinates of each electron will be a complex function of 3^N variables, rendering the demand for computational resources to increase beyond the pragmatic limit. For this reason, an approximation method called Density Functional Theory (DFT) [4] was developed.

This scheme simplifies many particle Schrödinger equations into an effective one-particle Schrödinger equation. Accordingly, the associated ground states properties of the system can be obtained from the ground state charge density expressed as

$$n(r) = \int \psi^*(r_1, r_2, \dots, r_n) \psi(r_1, r_2, \dots, r_n) dr_1, \dots, dr_n, \quad (2.12)$$

where r_N represents both spatial and spin coordinates. This shows that irrespective of the number of the electrons in the system the density of the system is always 3-dimensional. It is worth nothing that the electron density traced its history back in the 1920s by Thomas and Fermi (TF), but the model proposed fails to provide accurate ground energy as a result of inaccurate approximations made in kinetic energy [76]. However, it provides a hint that ground state energy can be determined using the electron density. It is based on the limitations of Thomas-Fermi model that Hohenberg-Kohn and Kohn-Sham [4, 66] proposed the DFT approach that gained popularity since 1970's.

The major advantage of DFT over the previously mentioned methods is the high numerical accuracy in treating a large system comprising hundreds of atoms at relatively low computational resources. But it has a shortcoming in treating van der Waals forces in the sparse material [66]. It also fails to correctly describe exchange and correlation interactions with great accuracy. This is the reason for continues formulation of several flavors of exchange and correlation functionals.

2.1.4 Fundamental of DFT

In 1964, Hohenberg-Kohn (HK) Theorem formulated a new idea which permits transformation of the total energy of N interacting particles as a function of the electron density $n(r)$ [66]. According to their statement, the ground state energy E_0 is a unique functional of the electron density $n(r)$. This means that there exists a direct relationship between external potential $V(r)$ of many interacting particles and electron

density $n(r)$. The second statement can be derived based on a simple variational principle. It shows a straightforward way to obtain exact ground state total energy and particle density of an interacting particle system as follows.

Suppose two potentials $V(r)$ and $V'(r)$ produce two electron densities $n(r)$ and $n'(r)$ at the ground state. Those potentials would have two distinct Hamiltonians H and H' whose ground state electron densities are equal but would have different normalized wave functions ψ and ψ' . Then, the ground state energy in terms of potential $V(r)$ can be expressed as

$$\begin{aligned}
 E_0' &= \langle \psi(r) | \hat{H}' | \psi(r) \rangle < \langle \psi(r) | \hat{H} | \psi(r) \rangle \\
 &< \langle \psi(r) | \hat{H} | \psi(r) \rangle + \langle \psi(r) | \hat{H}' - \hat{H} | \psi(r) \rangle \\
 &< E_0 + \int n(r) [V'(r) - V(r)] d^3r
 \end{aligned}
 \tag{2.13}$$

Similarly, ground state energy in terms of potential $V'(r)$ is written as

$$\begin{aligned}
 E_0 &= \langle \psi(r) | \hat{H} | \psi(r) \rangle < \langle \psi'(r) | \hat{H} | \psi'(r) \rangle \\
 &< \langle \psi'(r) | \hat{H} | \psi'(r) \rangle + \langle \psi'(r) | \hat{H} - \hat{H}' | \psi'(r) \rangle \\
 &< E_0' + \int n(r) [V(r) - V'(r)] d^3r
 \end{aligned}
 \tag{2.14}$$

The addition of equation (2.13) and equation (2.14) results in a contradictory argument

$$E_0 + E_0' < E_0 + E_0'. \tag{2.15}$$

This indicates that no two distinct external potentials can produce the same $n(r)$. This proves that the electronic density $n(r)$ is a unique functional of the potential $V(r)$. Further deduction from the expression (2.15) above is the possibility of relating the terms in the Hamiltonian as a functional of the electron density.

2.1.5 The Kohn-Sham (KS) Equation

The most important contribution that provides a practical realization of DFT approach as a numerical tool for real system is the work of Kohn-Sham (KS) [4] which was published a year after Hohenberg-Kohn theorem [66]. KS provides a possible to obtain electronic density in which the physical properties of a system depend on.

The fundamental idea was the mapping of the kinetic energy of interacting system onto an equivalent non-interacting system moving in an effective field. Subsequently, the introduction of exchange-correlation energy E_{XC} in a manner that non-interacting electrons have an equal ground state as the interacting electrons. According to their assumption, the error in the evaluation of K.E that leads to failure of Thomas Fermi model [77] could be avoided via the use of appropriate exchange-correlation potential. To derive Kohn-Sham equations, the Hamiltonian equation (2.3) is further separated into sum of functional that depends on the electron charge density expressed as

$$E_0[n(r)] = T_0[n(r)] + V_{\text{ext}}[n(r)] + V_{\text{elec-elec}}[n(r)] + E_{XC}[n(r)]. \quad (2.16)$$

where T_0 denotes the K.E of the system; the external potential $V_{\text{ext}}[n(r)]$ defined in the equation (2.16) is due to electrostatic interactions. $V_{\text{elec-elec}}[n(r)]$ is the electron-electron interaction potential and $E_{xc}[n(r)]$ exchange and correlation energy.

Recall Kohn-Sham assume that single particle S.E electron density can be expressed in terms of wave function

$$n(r) = \sum_{i=1}^N |\psi_i|^2, \quad (2.17)$$

The resulting K.E can be written as

$$T_0[n(r)] = -\frac{\hbar^2}{2m} \sum_i^N \langle \psi_i(r) | \nabla^2 | \psi_i(r) \rangle, \quad (2.18)$$

Where index i represent eigen state and r is any point in a real space with ψ_i constrained to be orthogonal *i.e.*,